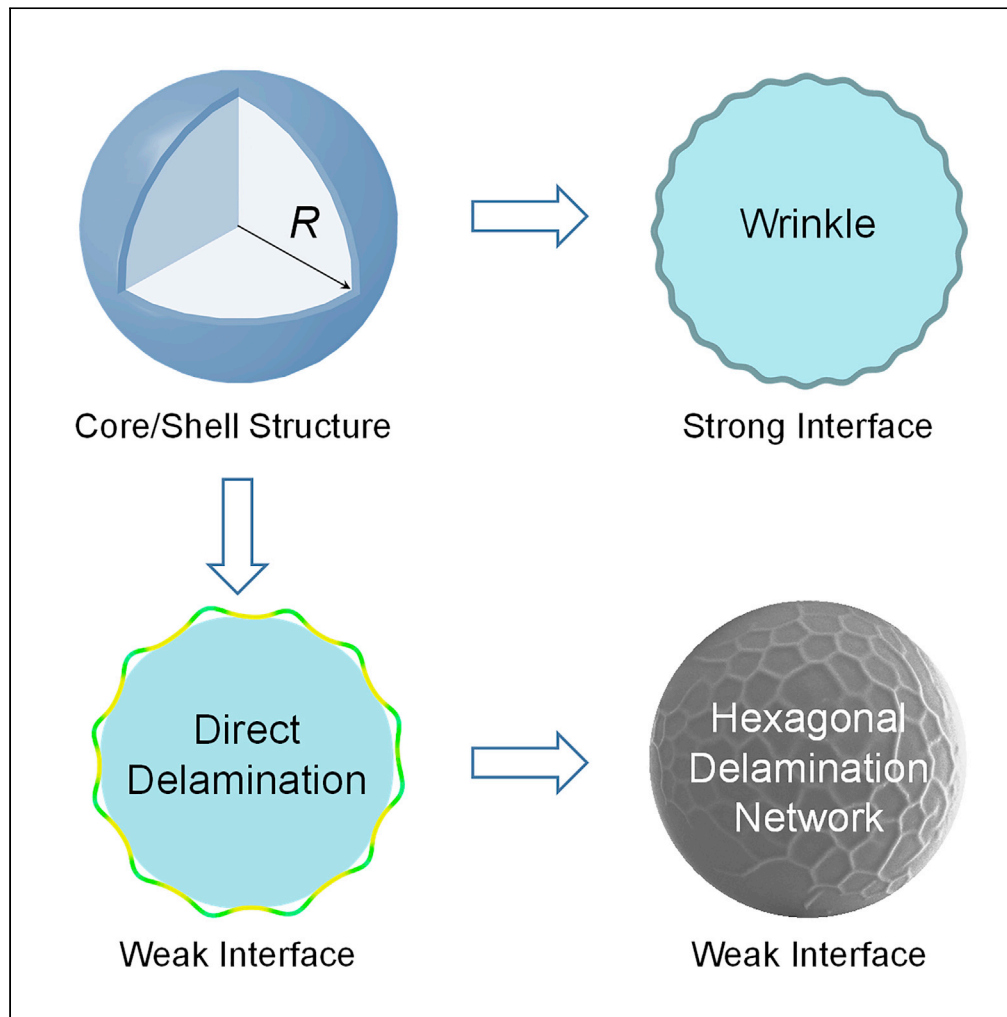


Article

# Curvature-controlled delamination patterns of thin films on spherical substrates



Liangliang Zhu,  
Haozhi Yuan, Kai  
Wu, ..., Jun Sun,  
Xiangbiao Liao, Xi  
Chen

liaoxiangbiao@gmail.com

**Highlights**

Delamination pattern emerges directly from the smooth sphere configuration

Weak adhesion results in a periodic delamination pattern of hexagonal dimples

Surface pattern can be controlled by substrate curvature and interfacial adhesion

Zhu et al., iScience 24, 102616  
June 25, 2021 © 2021 The  
Author(s).  
[https://doi.org/10.1016/  
j.isci.2021.102616](https://doi.org/10.1016/j.isci.2021.102616)



## Article

## Curvature-controlled delamination patterns of thin films on spherical substrates

Liangliang Zhu,<sup>1,4</sup> Haozhi Yuan,<sup>2,4</sup> Kai Wu,<sup>2</sup> Xueru Wang,<sup>2</sup> Gang Liu,<sup>2</sup> Jun Sun,<sup>2</sup> Xiangbiao Liao,<sup>3,5,\*</sup> and Xi Chen<sup>3</sup>

## SUMMARY

**Periodic delamination patterns in multilayer structures have exhibited extensive applications in microelectronics and optics devices. However, delamination behaviors of a closed thin shell on spherical substrates are still elusive. Herein, a unique instability mechanism of buckle delamination in a closed thin film weakly bonded to spherical substrates is studied by experiments, simulations, and theoretical analyses. The system of an Al film depositing on polystyrene spheres subjected to thermal mismatch strain is used for demonstration. Unlike traditional phenomena of wrinkling and wrinkle-induced delamination under increasing misfit strain, the weak adhesion between the core and shell results in a periodic pattern of delaminated hexagonal dimples that emerges directly from the smooth sphere configuration, before which no wrinkling occurs. Both substrate curvature and interfacial adhesion are revealed to control the dimple size and delamination width. These findings open a new venue for manifesting new controllable features for surface microfabrication.**

## INTRODUCTION

Film with residual compressive stress typically buckles and delaminates from a weakly bonded substrate. Stress-driven delamination was traditionally regarded as a failure mechanism in bilayer systems, and extensive efforts have been paid to investigate the intriguing delamination morphologies, including localized patterns of straight-sided, telephone-cord, varicose blisters and network-like patterns (Moon et al., 2004; Ni and Soh, 2014; Zhang and Arroyo, 2014). Through pre-patterning regions with weak adhesion, periodic delamination features over large areas have been controllably fabricated, which have attracted extensive applications in microelectronics and optics devices (Rogers et al., 2010). However, those strategies involved complex physicochemical/nanolithography techniques. Recently, spontaneous delamination arrays were realized by bonding a thin film to the pre-strained soft elastomeric substrate in the absence of pre-patterning (Vella et al., 2009; Zhang et al., 2017). These delamination patterns with high-aspect-ratio buckles outperformed wrinkling features in rich applications of flexible/stretchable electronics and surface-tunable properties (e.g., adhesion, wetting, and friction) (Thomas et al., 2015; Zang et al., 2013).

Despite significant progresses in delamination on planar surfaces, it is still unclear how the curvature effect and the topological constraint control the delamination pattern on curved geometries. It was well investigated that buckling patterns in shells and wrinkling features in core-shell bilayer systems are highly sensitive to geometries' curvatures. For example, labyrinthine and dent-like wrinkling topographies were observed in spherical elastic media with different radii (Cao et al., 2008; Li et al., 2011; Yuan et al., 2019). In addition, it was reported that the axial blister and circumferential blister occurred, respectively, on the inner and outer surfaces of a cylinder substrate due to the curvature-dependent energy release rate at delamination edges (Hutchinson, 2001). However, to the best of our knowledge, the mechanism of spontaneous delamination patterns on curved and closed substrate has not been revealed yet. Therefore, it is implied that the combination effect of curvature, interfacial adhesion, and topological constraints suggests more surface features beyond well-studied modes of instabilities (e.g., wrinkling, creasing, ridge, fold, and localized delamination) (Wang and Zhao, 2016). Herein, we analyze the spontaneous delamination patterns on a spherical core/shell structure through mismatched shrinkage/swell in volume. It is helpful to understand the patterns in biological systems, composite colloids, and crystallization of metal liquids, across a large scale, and the new controllable features for surface microfabrication could be exploited in applications of tunable friction (Yuan et al., 2019), adhesion (Li et al., 2021), wettability (Zhang et al., 2020), and optical transmittance (Thomas et al., 2015), to name a few.

<sup>1</sup>School of Chemical Engineering, Northwest University, Xi'an 710069, China

<sup>2</sup>State Key Laboratory for Mechanical Behavior of Materials, Xi'an Jiaotong University, Xi'an 710049, China

<sup>3</sup>Department of Earth and Environmental Engineering, Columbia University, New York, NY 10027, USA

<sup>4</sup>These authors contributed equally

<sup>5</sup>Lead contact

\*Correspondence: liaoxiangbiao@gmail.com  
<https://doi.org/10.1016/j.isci.2021.102616>



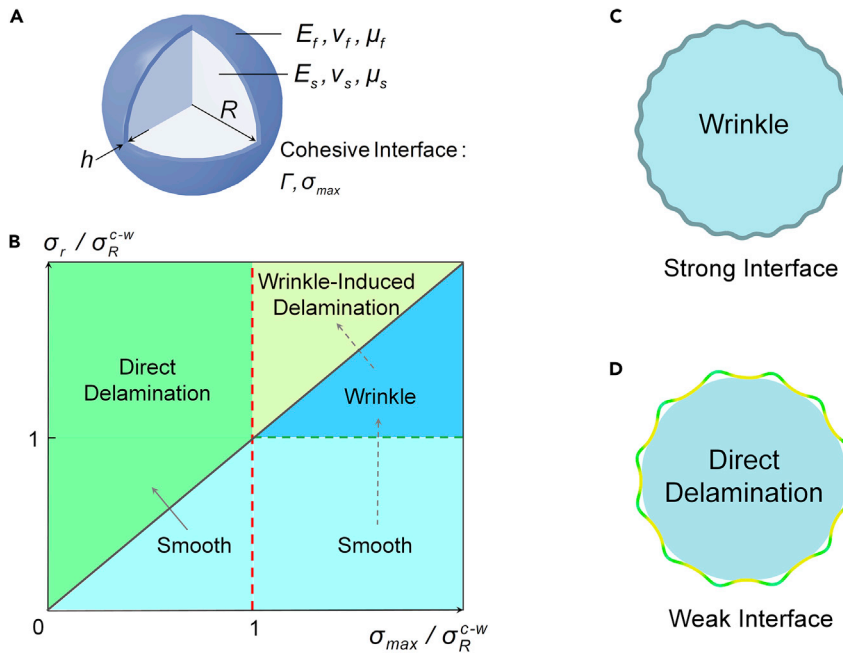


**Figure 1. Instability mechanism of the core shell system with a weak interface**

(A) Schematic of the core/shell model with a cohesive interface (see also Figure S1).

(B) Diagram of instability modes of the core/shell model (see also Figure S2).

(C) Cross section of the wrinkle morphology of the core/shell model with a strong interface.

(D) Cross section of the direct delamination morphology of the core/shell model with a weak interface.

## RESULTS AND DISCUSSION

### Onset and evolution of direct delamination patterns

We consider a core/shell structure (Figure 1A): a substrate with radius  $R$ , Young's modulus  $E_s$ , and Poisson's ratio  $\nu_s$  and a shell with thickness  $h$ , Young's modulus  $E_f$ , and Poisson's ratio  $\nu_f$ . The cohesive core/shell interface is characterized by the traction-separation model with normal and shear interfacial strength ( $\sigma_{max}$  and  $\tau_{max}$ , respectively) (Li and Suo, 2007; Zhang and Yin, 2018). The interfacial adhesion energy ( $\Gamma$  and  $\Gamma_s$  in the normal and shear direction, respectively, also referred to as the interfacial toughness) is the area under the traction-separation curve (see Figure S1) (Li and Suo, 2007; Zhang and Yin, 2018). The shear interfacial strength ( $\tau_{max}$ ) is usually very small for microscopic van der Waals interaction, and its variation in moderate range is not expected to influence the general buckling morphology (Zhang and Arroyo, 2014). Therefore, in the following, we mainly focus on the discussion on the normal interfacial strength ( $\sigma_{max}$ ). The interfacial debonding is initiated once the radial interfacial stress exceeds  $\sigma_{max}$ . The difference in thermal expansion coefficients for the film ( $\mu_f$ ) and substrate ( $\mu_s$ ,  $\Delta\mu = \mu_s - \mu_f > 0$ ) is adopted to generate mismatched shrinking when the whole structure is cooled down by a magnitude of  $\Delta T$ . Note that it would be of interest to investigate the loading strategies via other external stimuli (e.g., pH, humidity, and pneumatic pressure). Given the temperature drop,  $\Delta T$ , the radial interfacial stress in the film can be derived as (Cao et al., 2008),

$$\sigma_r(\Delta T) = \frac{2h}{R} \frac{E_f E_s (3R^3 + 3R^2 h + 3Rh^2 + h^3) (\mu_s - \mu_f) \Delta T}{3E_s(1 - \nu_f)R^3 + [E_s(1 + \nu_f) + 2E_f(1 - 2\nu_f)](3R^2 h + 3Rh^2 + h^3)} \quad (\text{Equation 1})$$

The critical radial stress for the onset of wrinkling ( $\sigma_R^{C-W}$ ) in the core/shell structure with a strong interface (Cai et al., 2011) is used to normalize the normal interfacial strength:  $\sigma_n = \sigma_{max} / \sigma_R^{C-W}$ , where  $\sigma_R^{C-W} = (h\bar{E}_f / 6/R)(3\bar{E}_s/\bar{E}_f)^{2/3}(\beta^2 + 2\beta^{-1} + 3Q^2\beta^{-2})$  with  $\beta^4 - \beta - 3Q^2 = 0$ .  $Q = (2h/R)(\bar{E}_f/3/\bar{E}_s)^{2/3}(1 - \nu_f^2)^{1/2}$  is a dimensionless parameter characterizing the curvature effect and moduli difference (Cai et al., 2011) and  $\bar{E}$  is the plane strain modulus ( $\bar{E} = E/(1 - \nu^2)$ ).

The diagram of instability modes in the core/shell structure with respect to the normalized radial stress ( $\sigma_r / \sigma_R^{C-W}$ ) and interfacial strength ( $\sigma_n = \sigma_{max} / \sigma_R^{C-W}$ ) is constructed in Figure 1B. With increasing  $\sigma_r$ ,

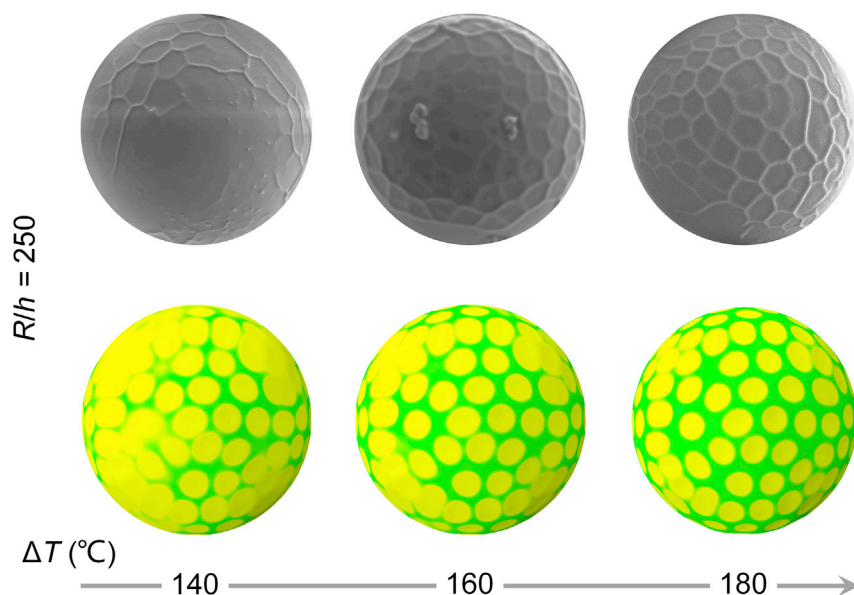


**Figure 2. Growing and spreading process of the hexagonal delaminated dimples on the spherical surface**

Here,  $R/h = 250$  and  $h = 50$  nm. The first row shows experimental results, and the second row shows simulation results. In the simulation results, the delaminated regions are depicted by green and the bonding regions by yellow.

(Equation 1), there are two pathways of the buckling pattern transition, depending on the interfacial strength. When the interface is tough ( $\sigma_n > 1$ , right half of Figure 1B), the smooth thin shell first deforms coherently with the substrate upon the temperature dropping (Figure 1C). With the interfacial stress  $\sigma_r$  exceeding the critical wrinkling stress ( $\sigma_R^{c-w}$ ), wrinkling phases of hexagonal, labyrinth, or hybrid features can be observed to be dependent on the substrate curvature, which have been well studied (Cao et al., 2008; Yuan et al., 2019). With increasing wrinkling amplitude, the wrinkle-induced delamination occurs once the radial stress approaches the normal interfacial strength. The wrinkle-to-delamination transition point depends on the stress state of the wave crest of the wrinkles on the curved surface, which, however, is very complex to theoretically deduce. We therefore left it for future studies.

However, in the case of a weak interface with  $\sigma_n < 1$  (left half of Figure 1B), the radial stress ( $\sigma_r$ ) reaches the interfacial strength ( $\sigma_{max}$ ) before the critical wrinkle stress ( $\sigma_R^{c-w}$ ) upon decreasing temperature. In this case, the smooth shell spontaneously debonds from the substrate and evolves into a direct delamination pattern (Figure 1D) dependent on the cooling temperature, substrate curvature, and adhesion strength, which are elucidated in the following.

To investigate the spontaneous delamination behavior in the case of weak interface, the shell/core microstructures were fabricated by depositing a layer of Al film on the polystyrene (PS) microsphere by the technique of magnetron sputtering, and parallel finite element simulations were conducted. Here,  $E_f = 70.0$  GPa,  $\nu_f = 0.346$ ,  $\mu_f = 2.32 \times 10^{-4} \text{C}^{-1}$ , and  $h = 50$  nm for the Al film and  $E_s = 3.0$  GPa,  $\nu_s = 0.350$ , and  $\mu_s = 8.00 \times 10^{-4} \text{C}^{-1}$  for the PS microsphere core. Through peeling tests, we obtained that  $\Gamma = 7.8 \text{ J m}^{-2}$ ,  $\sigma_{max} = 6.0 \text{ MPa}$ ,  $\Gamma_s = 0.78 \text{ J m}^{-2}$ , and  $\tau_{max} = 0.6 \text{ MPa}$  for the Al/PS interface, and thus the normalized interfacial strength in the PS core/Al shell system was found to be very small ( $\sigma_n \ll 1$ ). For example, in the case of  $R/h = 250$ , the critical wrinkle stress can be calculated as  $\sigma_R^{c-w} = 0.04 \text{ GPa}$ , which gives  $\sigma_n = \sigma_{max}/\sigma_R^{c-w} = 15\%$  ( $\ll 1$ ). We then cooled the core/shell systems from different temperatures to the room temperature, which was used to mimic the increasing load of compressive strain in the film. The consistent delamination pattern of hexagonal dimples (reminiscent of the structure of a buckliball [Lin et al., 2015]) was observed on the spherical substrate in both experiments and parallel simulations, as shown in Figure 2. With increasing temperature drop amplitude, the number of hexagonal dimples grew progressively from only a few dimples to full coverage of the spherical surface, during which the increment of the delamination width of the hexagon's edge is small. This implies that the strain energy in Al film is released preferentially through more delaminated hexagonal dimples rather than increasing the delamination width of

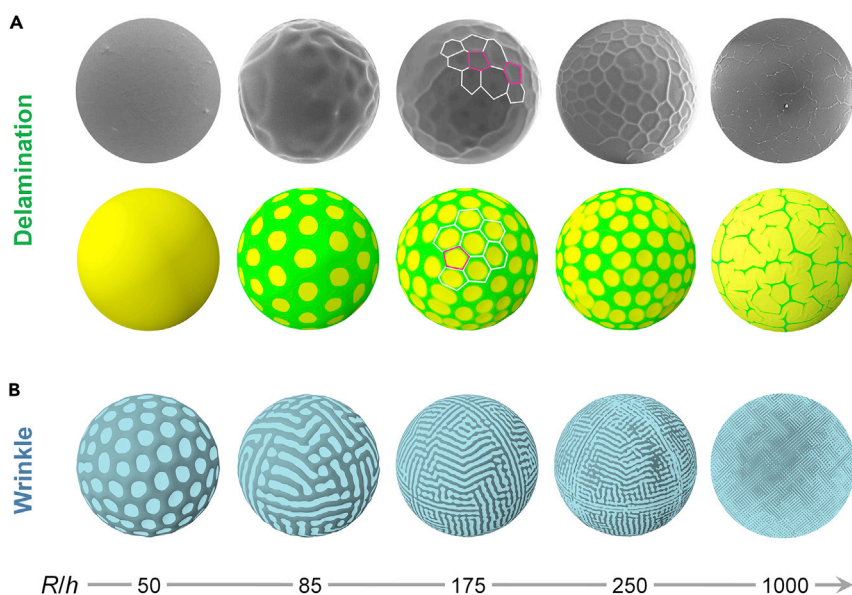


**Figure 3. Delamination patterns of the PS core/Al shell system with comparison to the wrinkle counterparts**

(A) Experiment (first row) and simulation (second row) delamination patterns of the core/shell system, obtained by a temperature drop of  $\Delta T = 180^\circ\text{C}$ . In the simulation results, the delaminated regions are depicted by green and the bonding regions by yellow.

(B) Simulated wrinkle patterns of the same systems with perfect interfaces (well-bonded throughout the simulation) obtained through a very large temperature drop ( $\Delta T = 1500^\circ\text{C}$ ), which is unrealistic and used in simulations only for morphology comparison. The last wrinkling case of  $R/h = 1,000$  has a very tiny wrinkle wavelength (relative to  $R$ ). In both (A) and (B), the shell thickness is  $h = 50$  nm.

the existing ones, until the dimples cover the whole spherical surface. In sharp contrast to the wrinkle-driven delamination where the wrinkling always precedes the delamination (Thomas et al., 2015; Vella et al., 2009), the direct delamination morphologies emerge directly from the sphere substrate without an earlier wrinkling process.

The morphologies of Al shell/PS core structures with different sizes were demonstrated in Figure 3A, where the temperature drop was fixed to be  $\Delta T = 180^\circ\text{C}$  in all cases. When the normalized radius of the substrate was moderate ( $R/h = 85, 175$ , and  $250$ ), all core/shell systems manifested a periodic pattern of delaminated hexagonal dimples. We also found a similar pattern in corresponding simulations. Several pentagonal topological defects were observed in the hexagonal lattice due to the closed and curved feature for the spherical surface (Jiménez et al., 2016), consistent with those patterns in the elastomeric hemispherical shell constrained by a rigid mandrel with a certain gap (Marthelot et al., 2017). These hexagons/pentagons are connected at the vertices, suggesting their potential application as microfluidic channels/networks (Moon et al., 2007). It is worth noting that the direct delamination pattern of hexagonal dimples was insensitive to the substrate's stiffness due to negligible deformation in the substrate, which is contrary to the wrinkling case (Cao et al., 2008; Yuan et al., 2019). Besides, the strategy of direct delamination from a spherical substrate is promising to achieve spontaneous pattern of hexagonal dimples in a wider range of geometric and material systems, compared with the wrinkling strategy. For example, when a well-bonded interface was applied (in simulation), only labyrinthine wrinkling patterns were obtained in the size of  $R/h \geq 85$  (Figure 3B), and the pattern became denser with increasing  $R/h$ . The dent-like wrinkling pattern with well-bonded interface was only achieved in the much smaller core/shell structure (e.g.,  $R/h = 50$ ) undergoing an extremely large temperature drop of  $\Delta T = 1500^\circ\text{C}$  (in simulation), whereas no buckling occurs in the case with the same size but weak interface (Figure 3). A tough core/shell interface was necessary to maintain the wrinkling pattern, otherwise further loading could result in a labyrinthine delamination pattern instead of keeping the hexagonal pattern in the case of  $R/h = 50$  (see Figures 1B and S2).

When the substrate radius was large, e.g.,  $R/h = 1000$ , we observed delaminated stripes with Y-shaped branches dominating the delamination pattern (Figure 3A). This pattern is somewhat reminiscent of the

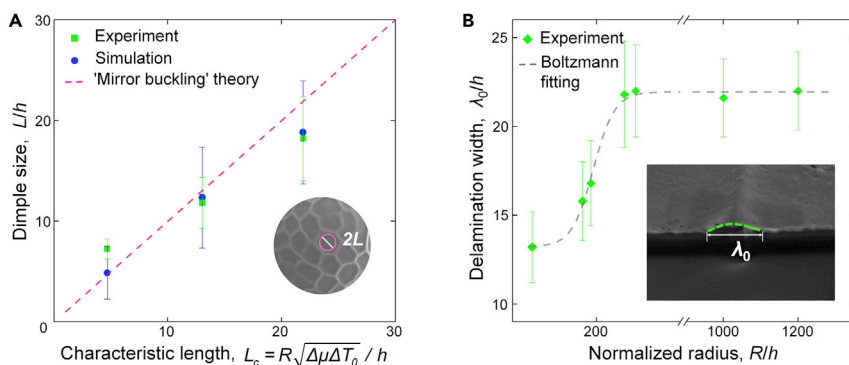


**Figure 4. Delamination size**

(A) Dimple size of the hexagonal delaminated dimples (see also Figure S3).

(B) Delamination width of the PS core/Al shell system with different sizes (see also Figures S4 and S5).

delamination morphology with abundant T-junctions in the system of graphene on a planar substrate (Zhang and Arroyo, 2014). Apparently, the substrate curvature has a significant influence on the delamination morphology, and the pattern of hexagonal dimples prefers to appear at a relatively small size.

However, no buckling was observed in both simulation and experiment when  $R/h$  was small (i.e., in the case of  $R/h = 50$  in Figure 3A), and a smooth spherical configuration of the outer shell was maintained during the cooling process. A theoretical model of a shell under external pressure was proposed (see method details) (Ventsel and Krauthammer, 2001) to predict the minimum normalized size of  $(R/h)_{cr}$  for the shell capable of buckling and delaminating from a spherical substrate:

$$(R/h)_{cr} = \sqrt{\frac{\alpha E_f}{\sigma_{max}}} \quad (\text{Equation 2})$$

where the coefficient  $\alpha$  varies between 0.31 and 1.23, depending on the initial imperfections of the sphere shell. For the present PS core/Al shell system, the minimum size can be narrowed within  $60 \leq (R/h)_{cr} \leq 120$ . This result is consistent with the phenomenon of no buckle delamination in the case of  $R/h = 50$ . Furthermore, the theoretical estimation was verified by the experimental evidence that the occurrence of the pattern of hexagonal delaminated dimples was random in cases of  $R/h = 85$  (see method details), and the randomness was possibly due to the geometric imperfections during the magnetron sputtering. For small core/shell systems, the small spherical shell is very stable and the critical buckling pressure ( $P_{cr}$ ) of the shell (free-standing) is larger than the normal interfacial strength ( $\sigma_{max}$ ). Therefore, upon temperature dropping, the radial interfacial stress ( $\sigma_r$ ) reaches  $\sigma_{max}$  first before it can make the shell buckle, causing global detachment between the shell and the core.

### Delamination size

The hexagonal pattern of direct delamination can be quantitatively characterized by two parameters: the size of dimples ( $L$ , defined as radius of the inscribed circle, inset in Figure 4A) and the initial delamination width ( $\lambda_0/h$ , inset in Figure 4B). The curvature effect on the dimple size was experimentally and theoretically illustrated in Figure 4A. The experimental/modeling results showed that  $L$  agrees well with the characteristic length of  $L_c = R\sqrt{\Delta\mu\Delta T_0}$  indicated by the “mirror buckling” theory (Gomez et al., 2016; Marthelot et al., 2017) (see method details and Figure S3).  $\Delta T_0$  is the temperature drop at which delamination initiates, and  $\Delta\mu\Delta T_0$  represents the mismatched compressive strain in the shell. Therefore, this result underpins that the dimple size in the direct delamination pattern could be controlled via the substrate curvature.

As shown in Figure 4B, the variation of the delamination width of  $\lambda_0/h$  is plotted as a function of the normalized radius of  $R/h$ , fitted with the Boltzmann function. With  $R/h$  increasing from 85 to 1,200 in the experiment, the normalized delamination width first increased exponentially and then reached a plateau of  $\lambda_0/h = 22.0$  after  $R/h = 250$ . For the case with large radius of curvature, the delamination width is expected to match that of a film delaminating from a planar stiff substrate:  $\lambda_0/h = \pi(2E_f h/I)^{1/4}$  (see method details). Given the parameters of  $E_f = 70.0$  GPa,  $\nu_f = 0.346$ ,  $h = 50$  nm, and  $I = 7.8$  J m<sup>-2</sup>, the theoretical

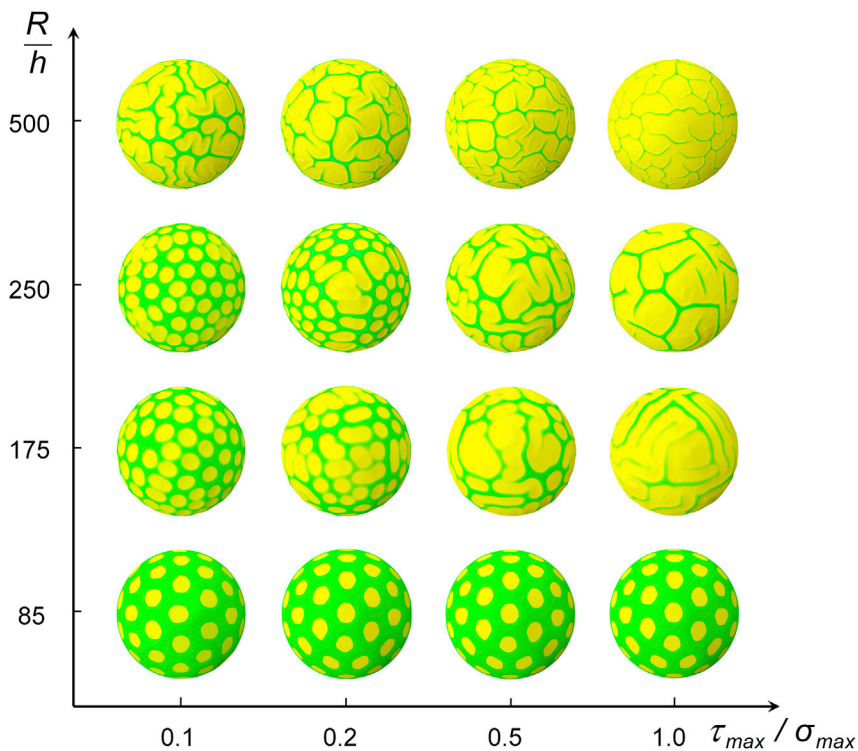


**Figure 5. Effect of normalized radius of curvature and shear interfacial strength on the delamination pattern**  
Results were obtained at  $\Delta T = 180^\circ\text{C}$ .

value of  $\lambda_0/h = 17.8$  moderately underestimates the delamination width compared with the experimental value at the plateau. The difference may be attributed to the neglect of stretching energy in the film and elastic energy in the substrate in the theoretical analysis. Moreover, we also developed a theoretical model based on the cylindrical core/shell system to characterize its delamination width (see [method details](#) and [Figure S4](#)). We obtained an analytic solution of the delamination width for the delaminated blisters on the cylindrical substrate, which showed the same trend with increasing  $R/h$ , that the delamination width soared to a plateau (see [Figure S5](#)).

### Dimple delamination pattern favors small shear interfacial strength

In addition to small  $R/h$ , we found that the dimple delamination pattern favors small shear interfacial strength ( $\tau_{max}$ ), whereas large  $\tau_{max}$  leads to the branching delamination pattern ([Figure 5](#)) analogous to the case with large  $R/h$  ([Figure 3](#)). For example, when the value of  $\tau_{max}$  is increased by 4 times (i.e.,  $\tau_{max}$  increases from  $0.1\sigma_{max}$  to  $0.5\sigma_{max}$ ), the dimple delamination pattern for  $R/h = 85$  is preserved, whereas for cases of  $R/h = 175$  and  $R/h = 250$ , the branching pattern takes over. When the propagation fronts of two close parallel delaminated stripes (propagating in opposite directions) meet, they tend to be attracted toward each other and may merge into one due to small values of the mode mixity ([Coupeau et al., 2019](#)). The elevated shear interfacial strength probably prevents the coalescence processes, leading to multiple Y-branches without forming hexagonal dimples.

Taking both the particle size and the shear interfacial strength into consideration, we can find that the dimple delamination pattern favors both small normalized radius of curvature ( $R/h$ ) and small shear interfacial strength ( $\tau_{max}$ ). When  $R/h$  is small enough (e.g.,  $R/h = 85$ ), the system keeps the dimple delamination pattern upon cooling regardless of the shear interfacial strength. When  $R/h$  is increased (e.g.,  $R/h = 175$  or  $250$ ), the hexagonal dimple pattern occurs only for small shear interfacial strength ( $\tau_{max}$ ); with  $\tau_{max}$  rising, the hexagonal dimple pattern breaks down gradually, evolving into a branching delamination pattern. Besides, the delamination stripes become sparser with increasing  $\tau_{max}$ , probably because of the mode mixity ([Hutchinson and Suo, 1991](#)) since a larger  $\tau_{max}$  significantly increases the energy penalty for crack

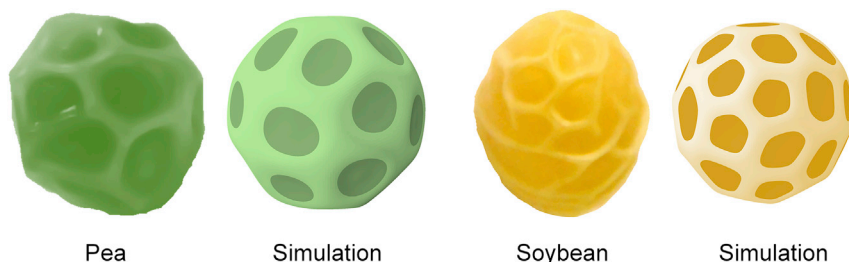


**Figure 6. Delamination pattern on beans with comparison to simulations**

The pea and the soybean have the same average radius ( $R = 3.5$  mm) but different seed coat thicknesses:  $h = 0.12$  and  $0.09$  mm, respectively. In the simulation, the material and interface properties are assumed to be:  $E_f = 10.0$  MPa,  $E_s = 1.0$  GPa,  $\nu_f = \nu_s = 0.3$ ,  $\mu_f = 2\mu_s = 0.002^\circ\text{C}^{-1}$ ,  $\Gamma = 7.8$  Jm $^{-2}$ ,  $\sigma_{max} = 10\tau_{max} = 0.015$  MPa, and  $\Delta T = 70^\circ\text{C}$  (increasing the temperature to mimic the water-absorption process).

propagation. Finally, for very large  $R/h$  (e.g.,  $R/h = 500$ ), the branching pattern appears all the time, even at a small value of  $\tau_{max}$ .

### Delamination pattern in biological sphere systems

The direct delamination pattern of the as-observed hexagonal dimples was also found in common biological systems. When dried peas and soybeans were immersed into hot water ( $90^\circ\text{C}$ ) for 3 min, the surface morphologies of such treated beans were captured as shown in Figure 6. While immersed in water, the bean skin, which is rich in starch, absorbed more water than the core of protein-rich cotyledon and resulted in a compressive strain in the bean skin. Owing to the weak interface, the bean skin delaminated from the cotyledon core and self-assembled into the pattern of hexagonal dimples, where the underlying mechanism was consistent with that in the Al shell/PS core system. Morphologies based on parallel simulations agreed well with those in the experiment. Although the size of soybeans was close to that of peas, the thinner skin in soybean led to smaller dimples in the hexagonal pattern (Figure 6), which matched the result in Figure 3A.

In summary, based on the PS core/Al shell system, both experimental and numerical analyses were carried out to investigate the effect of curvature and interfacial adhesion on the delamination patterns of thin films on spherical substrates. Two main delamination patterns have been observed, i.e., the dimple pattern, which is preferred for cases with small sizes (due to the strong curvature effect) and small shear interfacial strength, and the branching pattern, which dominates large systems. The critical buckling stress for delamination depends strongly on the interfacial strength, which may be remarkably smaller than the critical wrinkle stress of the same system. In this way, the delamination patterns emerge directly from the smooth sphere configuration without an earlier wrinkling process, which is in sharp contrast to the planar wrinkle-induced delamination behavior. Our findings provide new understandings to control the film buckling patterns on curved surfaces via substrate curvature and interfacial adhesion, which can be exploited in surface microfabrication for flexible electronics and biomedical and optics devices.

### Limitations of the study

In the theoretical analysis of the critical normalized curvature radius  $((R/h)_{cr})$ , a free-standing spherical shell under uniform external pressure ( $p$ ) is considered. For the core/shell model studied in the present work, the pressure exerted on the shell comes from core shrinking, and at the same time, the core provides a certain support for the shell, which may make it a little harder for the shell to buckle. Nevertheless, the "supporting effect" from the core is not considered to be significant enough to push the upper critical buckling load (which assumes a perfect shell) to a larger value. Based on the experiment and simulation results, we believe the above-deduced range for the minimum normalized size  $(R/h)_{cr}$  for buckling and delaminating holds for the core/shell system with weak interfaces.

### STAR★METHODS

Detailed methods are provided in the online version of this paper and include the following:

- KEY RESOURCES TABLE
- RESOURCE AVAILABILITY

- Lead contact
- Materials availability
- Data and code availability
- **METHOD DETAILS**
  - Preparation of PS microspheres
  - Preparation of Al shells
  - Characterization of interface
  - Characterization of delamination
  - Delamination on bean surfaces
  - Simulation
  - Critical radius of curvature for shell buckling
  - Delaminated dimple size
  - Delamination width

## SUPPLEMENTAL INFORMATION

Supplemental information can be found online at <https://doi.org/10.1016/j.isci.2021.102616>.

## ACKNOWLEDGMENTS

This work was supported by the National Natural Science Foundation of China (12002271, 11872302, 51801146, and 51625103), Xi'an Science and Technology Plan Project, China (2019220914SYS024CG046), and Earth Engineering Center and Center for Advanced Materials for Energy and Environment at Columbia University. We are appreciated for helpful suggestions from Prof. Yong Ni working at the University of Science and Technology of China.

## AUTHOR CONTRIBUTIONS

L.Z., X.L., and X.C. designed the study. L.Z. and X.L. were responsible for simulations and theoretical analysis. H.Y., L.Z., X.L., K.W., X.W., G.L., and J.S. conducted the experiments. All authors contributed to the writing of the manuscript.

## DECLARATION OF INTERESTS

The authors declare no competing interests.

Received: March 8, 2021

Revised: May 10, 2021

Accepted: May 19, 2021

Published: June 25, 2021

## REFERENCES

- Cai, S., Breid, D., Crosby, A.J., Suo, Z., and Hutchinson, J.W. (2011). Periodic patterns and energy states of buckled films on compliant substrates. *J. Mech. Phys. Sol.* *59*, 1094–1114.
- Cao, G., Chen, X., Li, C., Ji, A., and Cao, Z. (2008). Self-assembled triangular and labyrinth buckling patterns of thin films on spherical substrates. *Phys. Rev. Lett.* *100*, 036102.
- Coupeau, C., Boijoux, R., Ni, Y., and Parry, G. (2019). Interacting straight-sided buckles: an enhanced attraction by substrate elasticity. *J. Mech. Phys. Sol.* *124*, 526–535.
- Gomez, M., Moulton, D.E., and Vella, D. (2016). The shallow shell approach to Pogorelov's problem and the breakdown of 'mirror buckling'. *Proc. R. Soc. A Math. Phys. Eng. Sci.* *472*, 20150732.
- Hutchinson, J.W. (2001). Delamination of compressed films on curved substrates. *J. Mech. Phys. Sol.* *49*, 1847–1864.
- Hutchinson, J.W., and Suo, Z. (1991). Mixed mode cracking in layered materials. *Adv. Appl. Mech.* *29*, 63–191.
- Jiménez, F.L., Stoop, N., Lagrange, R., Dunkel, J., and Reis, P.M. (2016). Curvature-controlled defect localization in elastic surface crystals. *Phys. Rev. Lett.* *116*, 104301.
- Li, B., Jia, F., Cao, Y.P., Feng, X.Q., and Gao, H. (2011). Surface wrinkling patterns on a core-shell soft sphere. *Phys. Rev. Lett.* *106*, 234301.
- Li, Q., Zhang, P., Yang, C., Duan, H., and Hong, W. (2021). Switchable adhesion between hydrogels by wrinkling. *Extreme Mech. Lett.* *43*, 101193.
- Li, T., and Suo, Z. (2007). Ductility of thin metal films on polymer substrates modulated by interfacial adhesion. *Int. J. Sol. Structures* *44*, 1696–1705.
- Lin, S., Xie, Y.M., Li, Q., Huang, X., and Zhou, S. (2015). Buckling-induced retraction of spherical shells: a study on the shape of aperture. *Sci. Rep.* *5*, 11309.
- Marthelot, J., Brun, P.T., Jiménez, F.L., and Reis, P.M. (2017). Reversible patterning of spherical shells through constrained buckling. *Phys. Rev. Mater.* *1*, 025601.
- Mei, H., Landis, C.M., and Huang, R. (2011). Concomitant wrinkling and buckle-delamination of elastic thin films on compliant substrates. *Mech. Mater.* *43*, 627–642.
- Moon, M.-W., Chung, S., Lee, K.-R., Oh, K.H., Stone, H.A., and Hutchinson, J.W. (2007). Directed assembly of fluidic networks by buckle

delamination of films on patterned substrates. *Int. J. Mater. Res.* 98, 1203–1208.

Moon, M.W., Lee, K.R., Oh, K.H., and Hutchinson, J.W. (2004). Buckle delamination on patterned substrates. *Acta Mater.* 52, 3151–3159.

Ni, Y., and Soh, A.K. (2014). On the growth of buckle-delamination pattern in compressed anisotropic thin films. *Acta Mater.* 69, 37–46.

Rogers, J.A., Someya, T., and Huang, Y. (2010). Materials and mechanics for stretchable electronics. *Science* 327, 1603–1607.

Thomas, A.V., Andow, B.C., Suresh, S., Eksik, O., Yin, J., Dyson, A.H., and Koratkar, N. (2015). Controlled crumpling of graphene oxide films for tunable optical transmittance. *Adv. Mater.* 27, 3256–3265.

Vella, D., Bico, J., Boudaoud, A., Roman, B., and Reis, P.M. (2009). The macroscopic delamination of thin films from elastic substrates. *Proc. Natl. Acad. Sci. U S A* 106, 10901–10906.

Ventsel, E., and Krauthammer, T. (2001). *Thin Plates and Shells: Theory Analysis and Applications* (Marcel Dekker).

Wang, Q., and Zhao, X. (2016). Beyond wrinkles: multimodal surface instabilities for multifunctional patterning. *MRS Bull.* 41, 115–122.

Yuan, H., Wu, K., Zhang, J., Wang, Y., Liu, G., and Sun, J. (2019). Curvature-controlled wrinkling surfaces for friction. *Adv. Mater.* 31, e1900933.

Zang, J., Ryu, S., Pugno, N., Wang, Q., Tu, Q., Buehler, M.J., and Zhao, X. (2013). Multifunctionality and control of the crumpling and unfolding of large-area graphene. *Nat. Mater.* 12, 321–325.

Zhang, H., Zhu, H., Liang, X., Liu, P., Zhang, Q., and Zhu, S. (2020). Wrinkled smart surfaces: enhanced switchable wettability and directional liquid transportation. *Appl. Surf. Sci.* 513, 145810.

Zhang, K., and Arroyo, M. (2014). Understanding and strain-engineering wrinkle networks in supported graphene through simulations. *J. Mech. Phys. Sol.* 72, 61–74.

Zhang, Q., Tang, Y., Hajfathalian, M., Chen, C., Turner, K.T., Dikin, D.A., Lin, G., and Yin, J. (2017). Spontaneous periodic delamination of thin films to form crack-free metal and silicon ribbons with high stretchability. *ACS Appl. Mater. Interfaces* 9, 44938–44947.

Zhang, Q., and Yin, J. (2018). Spontaneous buckling-driven periodic delamination of thin films on soft substrates under large compression. *J. Mech. Phys. Sol.* 118, 40–57.

## STAR★METHODS

### KEY RESOURCES TABLE

REAGENT or RESOURCE	SOURCE	IDENTIFIER
Software and Algorithms		
Abaqus 6.17	Provided by Dassault Systèmes	N/A

### RESOURCE AVAILABILITY

#### Lead contact

Further information and requests for resources should be directed to and will be fulfilled by the lead contact, Xiangbiao Liao ([iaoxiangbiao@gmail.com](mailto:iaoxiangbiao@gmail.com)).

#### Materials availability

This study did not generate new unique reagents.

#### Data and code availability

This study did not generate/analyze datasets/code.

### METHOD DETAILS

#### Preparation of PS microspheres

Firstly, the polyvinylpyrrolidone (PVP) was dissolved in the 90% ethanol aqueous with mechanical stirring over 30 min at a temperature of 70°C. Then, the azodiisobutyronitrile (AIBN) dissolved in styrene monomer was added. The stirring and the temperature was kept for 24 h under nitrogen condition and the sample was then cooled. The monodisperse PS micro particles were obtained by centrifuging the reaction mixture, decanting the supernatant, and washing the particles in ethanol and deionized water. Through adjusting initial monomer concentrations, PS micro particles with different sizes were obtained.

#### Preparation of Al shells

Al films with a thickness of 50 nm were deposited on the prepared PS microspheres through direct current magnetron sputtering inside a chamber at different temperatures with base pressure kept at  $\sim 5 \times 10^{-5}$  Pa. The power was fixed at 200 W, and the Argon pressure 1.0 Pa. To ensure film uniformity, the core substrate was rotated at a speed of 20 r.p.m. during sputtering, after which the sample were hold for 2 h to cool down to room temperature (20°C).

#### Characterization of interface

The interface between the Al film and the PS core can be characterized by a tensile and a shear traction-displacement law (see [Figure S1](#)) (Li and Suo, 2007), with four parameters: the normal interfacial strength ( $\sigma_{max}$ ) and toughness ( $I$ ), and the shear interfacial strength ( $\tau_{max}$ ) and toughness ( $I_s$ ). In a peeling test, the normal interfacial toughness can be expressed as  $I = P_f^2 / (2E_f w_f^2 h) + P_f / [w_f (1 - \cos\theta)]$ , where  $E_f$ ,  $w_f$  and  $h$  are the Young's modulus, width and thickness of the film, respectively, and  $P_f$  is the force required to pull off the film from the substrate at an angle  $\theta$  (Zhang and Yin, 2018). By a peeling test of an Al film with  $h = 310$  nm,  $w_f = 6.42$  mm,  $E_f = 70.0$  GPa from a PS substrate at the peel angle of  $\theta = 90^\circ$ , we obtained  $P_f = 0.05$  N, and thus  $I = 7.8$  J m<sup>-2</sup>. We further conducted pull-out tests to measure the normal and shear interfacial strength. Al film with  $h = 310$  nm was deposited on one surface of a  $1 \times 1 \times 1$  cm<sup>3</sup> PS cube, which was then adhered to the PS substrate by epoxy resin as glue ([Figure S1](#)). The lower PS substrate was fixed and the upper PS cube was clamped and pulled in the normal or shear direction. By pull-out tests, the normal and shear interfacial strength were measured to be  $\sigma_{max} = 6.0$  MPa and  $\tau_{max} = 0.6$  MPa, respectively, and the shear interfacial toughness were thus estimated to be  $I_s = 0.78$  J m<sup>-2</sup>, the variation of which in moderate range (in simulations) has little influence on the results.

### Characterization of delamination

Surface morphologies of the above samples were characterized by SEM (HITACHI SU6600) and AFM. The dimple size and delamination width were statistically obtained from the AFM measurements.

### Delamination on bean surfaces

Dried beans (peas and soybeans) were immersed into 90°C water for 3 min. Room temperature water worked as well but it took longer time for the delamination pattern to appear. Surface morphologies of the beans taken out of the water were captured by camera. If immersed for longer time, the interface between the seed coat and the core would be destroyed by water and the delamination pattern would disappear gradually.

### Simulation

A core/shell structure with a weakly and uniformly bonded interface (Figure S1) is considered. A cohesive interface interaction model (not cohesive elements) is employed which simplifies the usually nonlinear interface behavior (e.g., van der Waals interface) into a bilinear cohesive law (Zhang and Yin, 2018), while retaining the well depth of adhesion energy,  $\Gamma$  and  $\Gamma_s$ , and the maximum normal/shear interface pressure,  $\sigma_{max}$  and  $\tau_{max}$  (Figure S1). Commercial finite element software ABAQUS is used to carry out the 3D simulations exploiting the bilinear cohesive interface model and using the dynamic explicit solver. Shell elements (S4R, 4-node quadrilateral shell element with reduced integration) and solid elements (C3D8R, 8-node brick element with reduced integration) are used to discretize the film and substrate, respectively. Mesh density of the spherical substrate is gradually increased in the radial direction to save computational cost. Without over-resolving the problem, appropriate mesh density is ensured through convergence studies. Specific geometrical and material parameters are based on the experimental Al/PS systems. Taking one case for example, geometrical and material parameters for the Al shell are  $h=50$  nm,  $E_f=70.0$  GPa,  $\nu_f=0.346$ ,  $\mu_f=2.32 \times 10^{-4} \text{°C}^{-1}$ ; for the PS core,  $R=12.5$   $\mu\text{m}$ ,  $E_s=3.0$  GPa,  $\nu_s=0.350$  and  $\mu_s=8.00 \times 10^{-4} \text{°C}^{-1}$ ; and for the interface,  $\Gamma=7.8$  J m<sup>-2</sup>,  $\sigma_{max}=6.0$  MPa,  $\Gamma_s=0.78$  J m<sup>-2</sup> and  $\tau_{max}=0.6$  MPa. In the wrinkle simulation (Figure 3B), the shell and the substrate are tied together, i.e., a perfect interface is employed. The temperature of the system is cooled down by a magnitude of  $\Delta T$  to induce the delamination/wrinkling patterns. The obtained delamination/wrinkle pattern is fully reversible in simulation after the loading is removed. And expanding instead of shrinking the system, while exchanging the thermal expansion coefficients of the film and the substrate, leads to the same results.

### Critical radius of curvature for shell buckling

Considering a closed spherical shell under uniform external pressure ( $p$ ), based on the linear buckling analysis, the governing stability equation is (Ventsel and Krauthammer, 2001),

$$D\nabla^6 w + \frac{pR}{2}\nabla^4 w + \frac{E_f h}{R^2}\nabla^2 w = 0 \quad (\text{Equation 3})$$

where  $w$  is the radial deflection and  $D = E_f h^3 / [12(1 - \nu_f^2)]$  is the flexural stiffness. Assuming the solution satisfies  $\nabla^2 w = -\xi^2 w$  yields the following equation ( $\xi \neq 0$ ),

$$\left( D\xi^4 - \frac{pR}{2}\xi^2 + \frac{E_f h}{R^2} \right) \xi^2 w = 0 \quad (\text{Equation 4})$$

Solving this equation, one obtains,

$$p = \frac{2E_f h}{R^3 \xi^2} + \frac{2D}{R} \xi^2 \quad (\text{Equation 5})$$

Taking the limit of  $p$  with respect to  $\xi^2$  ( $dp/d(\xi^2) = 0$ ), we have  $\xi^2 = \sqrt{E_f h / (DR^2)} = \sqrt{12(1 - \nu_f^2) / (Rh)}$ , substituting which into Equation 5 leads to the critical buckling pressure as (Ventsel and Krauthammer, 2001),

$$p_{cr}^{(1)} = \frac{2}{\sqrt{3(1 - \nu_f^2)}} E_f (h/R)^2 \quad (\text{Equation 6})$$

For  $\nu_f = 0.346$ , we have  $p_{cr}^{(1)} = 1.23E_f(h/R)^2$ . Equation 6 is considered as the "upper" critical buckling load as the shell is assumed to be perfect, while an actual spherical shell is sensitive to even the slightest initial

imperfections. By considering the nonlinear stability analysis for the spherical shell, which is extremely complicated, one obtains,

$$p_{cr}^{(2)} = 0.31E_f(h/R)^2 \quad (\text{Equation 7})$$

which is considered as the "lower" critical buckling load (Ventsel and Krauthammer, 2001). The real critical buckling load  $p_{cr}$  is usually somewhere between  $p_{cr}^{(1)}$  and  $p_{cr}^{(2)}$ , i.e.,  $p_{cr}^{(1)} \leq p_{cr} \leq p_{cr}^{(2)}$ , and the critical normalized radius of curvature  $((R/h)_{cr})$ , can be deduced by  $p_{cr} = \sigma_{max}$ , which gives  $60 \leq (R/h)_{cr} \leq 120$  for the PS core/Al shell system. In the experiments, when  $R/h$  was around 85, some cases showed the buckling morphology while some did not, which may be attributed to the different imperfections of the shells during magnetron sputtering. Therefore, we determined the experimental critical radius of curvature for buckling as  $R/h = 85$ , which is located in the middle of the above obtained theoretical range.

### Delaminated dimple size

The 'mirror buckling' theory assumes that, when a sphere shell is 'poked' by a force,  $F$ , a portion of the shell inverts to become an identical but inverted spherical cap compared to its original shape. The radius of the inverted cap can be deduced through simple trigonometry, which gives  $r \approx \sqrt{R\delta}$  (see Figure S3). This equation is employed to characterize the size of delaminated dimples in the present work. Here we take  $\delta$  to be the mismatched shrinking distance between the shell and the core, i.e.,  $\delta = R\Delta\mu\Delta T_0$ , thus we have  $L_c = R\sqrt{\Delta\mu\Delta T_0}$ , where  $\Delta T_0$  is the temperature drop at which delamination initiates.

### Delamination width

For large values of  $R/h$ , the occurring of interfacial delamination is analog to that of a planar elastic film on a rigid substrate (since the substrate deformation is minimal here), in which case the energy release rate ( $G$ ) driving the growth of delamination is  $G = \bar{E}_f h \epsilon^2 / 2$ , where  $\epsilon$  is the nominal compressive strain of the film (Mei et al., 2011). Triggered by the radial interfacial stress exceeding the interfacial strength, the delamination initiates and arrests as the energy release rate is balanced by the interfacial toughness, i.e.,  $G = \Gamma$ . The relationship between the delamination width ( $\lambda$ ) and nominal compressive strain has been determined as  $\lambda = \pi h \sqrt{\bar{E}_f h \epsilon / \Gamma}$ , through an energy-based mechanics analysis (Zhang and Yin, 2018). The initial delamination width can thus be obtained as,

$$\lambda_0 / h = \pi \left( 2\bar{E}_f h / \Gamma \right)^{1/4} \quad (\text{Equation 8})$$

Equation 8 gives  $\lambda_0/h = 17.8$  for the present system which is moderately below the experimental value. The difference may be attributed to the neglect of the stretching energy of the film and the strain energy in the substrate during the energy-based analysis (Zhang and Yin, 2018).

Besides, in the following, we develop a theoretical mechanics model based on the cylindrical core/shell system to characterize its delamination width (see Figure S4). Assuming  $A \ll \lambda_0 \ll R$  and neglecting the stretching energy in the film and the strain energy in the substrate (they can be reasonably neglected because of their small value compared to other energy terms), the total energy in one delamination blister (Figure S4B) of the cylindrical core/shell system can be written as (Zhang and Yin, 2018),

$$U_{total} = U_{bend} + U_{adhesion} = \frac{\pi^4 \bar{E}_f h^3 A^2}{12\lambda_0^3} + \frac{\Gamma\lambda_0}{1 - \epsilon} \quad (\text{Equation 9})$$

where  $U_{bend}$  is the bending energy of the blister,  $U_{adhesion}$  is the interfacial adhesion energy and  $\epsilon$  is nominal compressive strain of the blister in the hoop direction. By minimizing the total potential energy with respect to  $\lambda_0$ , we can obtain the equilibrium profile of the blister, i.e.,

$$\frac{dU_{total}}{d\lambda_0} = 0 \quad (\text{Equation 10})$$

Based on the geometry of one delamination blister (see Figure S4), the shape of the blister can be described as  $\rho(\theta) = R + A/2 \cdot [1 - \cos(2\pi R\theta / \lambda_0)]$  ( $0 \leq \theta \leq \lambda_0/R$ ), and thus the geometric relationship can be given by,

$$l_0 = \int_0^{\lambda_0/R} \sqrt{\rho^2(\theta) + \rho'^2(\theta)} d\theta = \lambda_0 \left( \frac{A/2 + R}{R} \right) \left[ 1 + \frac{\pi^2 A^2}{4\lambda_0^2} \left( \frac{R}{A/2 + R} \right)^2 \right] = \frac{\lambda_0}{1 - \epsilon} \quad (\text{Equation 11})$$

where  $l_0$  is the arc length of the blister.

Combining Equations 10 and 11, the delamination width of the delaminated blister can be derived as,

$$\lambda_0 = \frac{2\pi R \sqrt{\varepsilon - \varepsilon^2}}{\left\{ (2H - 1)/3 + \left[ -Q/2 + \sqrt{(Q/2)^2 + (P/3)^3} \right]^{1/3} + \left[ -Q/2 - \sqrt{(Q/2)^2 + (P/3)^3} \right]^{1/3} \right\}^{1/2}} \quad (\text{Equation 12})$$

where  $H = 1 + (1 - 2\varepsilon)^2 + 12\Gamma R^2(1 - \varepsilon)/(\bar{E}_f h^3)$ ,  $P = -(1 + H)^2/3$ , and  $Q = 2(1 + H)^3/27 - 4(1 - 2\varepsilon)^2$ .

Taking  $E_f = 70.0$  GPa,  $\nu_f = 0.346$ ,  $h = 0.05$   $\mu\text{m}$ ,  $\Gamma = 7.8$  J/m<sup>2</sup>, and  $\varepsilon = \Delta\mu\Delta T = 5.68 \times 10^{-4} * 180$  (a rough estimation based on Figure 3), the relationship between the delamination width,  $\lambda_0/h$ , and the size of the cylindrical core/shell system,  $R/h$ , can be plotted as shown in Figure S5.